Am J Cancer Res 2025;15(8):3395-3416
www.ajcr.us /ISSN:2156-6976/ajcr0165191

Original Article

LncRNA MIR31HG facilitates immune escape in head and neck squamous cell carcinoma by promoting heterotypic cell-in-cell formation

Qigen Fang[1], Junhui Yuan[2], Xu Zhang[2], Lisong Lin[1]

[1]*Department of Oral and Maxillofacial Surgery, School and Hospital of Stomatology, Fujian Medical University, No. 246, Yangqiao Middle Road, Gulou District, Fuzhou 35000, Fujian, P. R. China;* [2]*The Affiliated Cancer Hospital of Zhengzhou University and Henan Cancer Hospital, Zhengzhou 450008, Henan, P. R. China*

Received April 9, 2025; Accepted August 3, 2025; Epub August 15, 2025; Published August 30, 2025

Abstract: The aggressive nature of head and neck squamous cell carcinoma (HNSCC) is profoundly shaped by a complex interplay between malignant cells and the host immune system. A key feature of this interplay is the formation of cell-in-cell (CIC) structures, which facilitate immune evasion and contribute to shaping the tumor microenvironment. Long non-coding RNAs (lncRNAs), including MIR31HG, have emerged as crucial modulators of tumor immunity and metastasis. In this study, we investigated the role of MIR31HG in orchestrating heterotypic CIC formation and assessed its impact on tumor growth, immune surveillance, and chemoresistance in HNSCC. Analysis of TCGA and GTEx datasets confirmed the differential expression of CIC-related genes between HNSCC and normal tissues. Functional assays demonstrated that CIC structure formation substantially augmented the malignant properties of Cal27 cells, including increased resistance to both cisplatin and gemcitabine. Critically, genetic depletion of MIR31HG in CIC-positive cells (CIC^+ sh-MIR31HG) potently suppressed tumor progression, as evidenced by reduced cell proliferation and increased apoptosis. Furthermore, silencing MIR31HG also remodeled the immunosuppressive landscape; it downregulated the expression of immune checkpoint protein PD-L1 and decreased the secretion of immunosuppressive cytokines TGF-β and IL-10. This intervention also reversed therapeutic resistance, rendering CIC^+ sh-MIR31HG cells more susceptible to cisplatin- and gemcitabine-induced apoptosis. These findings were validated in a murine xenograft model, where histological analyses confirmed that tumors originating from CIC^+ sh-MIR31HG cells displayed reduced volume and elevated apoptotic activity. Collectively, MIR31HG is a pivotal regulator of heterotypic CIC formation in HNSCC. This mechanism promotes HNSCC cell survival, fosters an immunosuppressive microenvironment, and drives chemoresistance. Therefore, targeting MIR31HG represents a viable therapeutic avenue to disrupt immune resistance and enhance chemosensitivity in HNSCC.

Keywords: Head and neck squamous cell carcinoma, cell-in-cell structures, lncRNA MIR31HG, tumor microenvironment

Introduction

Head and neck squamous cell carcinoma (HNSCC) encompasses a heterogeneous group of malignancies originating from epithelial tissues, including the pharynx. It is currently the seventh most prevalent cancer worldwide, with incidence forecasted to increase by approximately 30% by 2030 [1]. The prognosis of HNSCC is frequently undermined by high rates of local recurrence and distant metastasis; over 50% of patients experience disease progression within three years after diagnosis [2]. The lungs are the predominant site of distant spread, accounting for 70-85% of all metastatic cases [3]. Despite the established therapeutic modalities (surgery, radiotherapy, and chemotherapy), outcomes for patients with recurrent or metastatic (R/M) disease remain dismal. Notably, the 5-year survival rate for HNSCC remained largely unchanged over the past three decades, underscoring an urgent need for improved therapeutic paradigms [4].

Long non-coding RNAs (lncRNAs), regulatory transcripts exceeding 200 nucleotides in length without protein-coding capacity, have emerged as key contributors to cancer pathogenesis and

https://doi.org/10.62347/MMZP1913

are distributed in both the nucleus and cytoplasm [5]. Increasing evidence has linked dysregulated lncRNAs expression and cancer development [6]. One such molecule, MIR31HG, a lncRNA composed of 2166 nucleotides, has been identified as a potent oncogenic factor in several cancers, including non-small cell lung cancer (NSCLC), hepatocellular carcinoma, and pancreatic cancer [7, 8]. In the context of head and neck cancers, Huang et al. reported that MIR31HG plays a crucial role in the carcinogenesis of areca nut-induced HNC [9]. Furthermore, Feng et al. revealed a significant association between high MIR31HG expression and aggressive clinicopathological characteristics in nasopharyngeal carcinoma (NPC) [10]. Their work further revealed that silencing MIR31HG inhibited cancer cell viability and colony formation, promoted apoptosis, and suppressed the PI3K/AKT signaling pathway by downregulating the levels of p-PI3K and p-AKT.

A distinct pathological feature frequently observed in HNSCC and other tumors is the formation of cell-in-cell (CIC) structures, where one or more viable cells are internalized by a host cell [11]. This process is often a prelude to the death of the internalized cell, which is typically degraded by the host. First described in tumor biology, CIC formation has been implicated in tumor progression, metastatic dissemination, and immune evasion [12]. These structures have been widely reported across multiple malignancies, and in HNSCC, the interaction between tumor and immune cells within CIC structures is particularly relevant to the tumor's immune escape mechanisms [13].

CICs are broadly categorized into two principal subtypes. The first, homotypic CIC, also known as entosis, involves the engulfment of one tumor cell by another [14, 15]. This interaction, often driven by microenvironmental factors such as nutrient deprivation or mechanical stress, typically culminates in the apoptotic death of the internalized cell, thereby influencing tumor architecture and cellular dynamics [16]. The second subtype, heterotypic CICs, has garnered significant interest in cancer immunology. It involves the internalization of immune cells by tumor cells. Aggressive cancers like HNSCC can actively engulf immune effector cells, including T lymphocytes and natural killer (NK) cells, sequestering them within vacuoles for subsequent elimination [17-19]. This phenomenon represents a potent mechanism of immune evasion, allowing tumors to thrive despite an active immune response. The engulfed immune cells typically undergo apoptotic death, which not only suppresses immune surveillance but may also contribute to tumor cell survival and resistance to immunotherapies [20].

The molecular mechanism underlying CIC formation is intricate, involving dynamic cytoskeletal rearrangements, autophagy, and the formation of large internal vacuoles [21]. Once internalized, cells are subjected to pro-death signaling cascades, including caspases activation and engagement of the NLRP3 inflammasome, ultimately leading to their degradation [15, 22]. In the specific landscape of HNSCC, which is often characterized by chronic inflammation and viral infections (e.g., HPV), the tumor microenvironment appears particularly conducive to CIC development [23, 24]. Consequently, this phenomenon is postulated not only to facilitate immune escape but also to enhance metastatic potential by remodeling the tumor microenvironment. Moreover, emerging evidence suggests that CIC structures may contribute to resistance to both chemotherapy and radiotherapy, potentially providing protective niches for tumor cell survival [11, 25].

In summary, the expression of the lncRNA MIR31HG and the formation of CIC structures are both implicated in the complex pathobiology of HNSCC, influencing tumor progression and immune interaction. However, the potential regulatory role of MIR31HG in heterotypic CIC formation remains unexplored. This study aims to clarify the regulatory function of MIR31HG in heterotypic CIC assembly and to map its downstream effects on tumor immune evasion and behavior. By elucidating this mechanism, we seek to establish a theoretical foundation for identifying novel therapeutic targets. We hypothesize that targeting MIR31HG may offer a promising strategy to reverse immune suppression and enhance the efficacy of current and future therapies for HNSCC.

Materials and methods

Patient information

All samples in this study were sourced from the Affiliated Cancer Hospital of Zhengzhou

University & Henan Cancer Hospital, collected between January and April 2024. The study protocol was approved by the Ethics Committee of Henan Cancer Hospital. Patient information is detailed in **Table 1**.

Data acquisition and gene expression analysis

To characterize the expression landscape of genes associated with cell-in-cell (CIC) structures in HNSCC, we performed a comprehensive bioinformatic analysis using publicly available datasets. Differential expression profiles of CIC-related genes was first assessed by comparing HNSCC tumor samples from The Cancer Genome Atlas (TCGA) against normal tissue samples from both TCGA and the Genotype-Tissue Expression (GTEx) project. This comparative analysis was executed using the Gene Expression Profiling Interactive Analysis (GEPIA) web platform to identify transcriptional alterations significantly associated with malignant transformation.

To further explore the clinical relevance of these expression patterns, we analyzed the TCGA-HNSCC dataset using the University of Alabama at Birmingham Cancer data analysis portal (UALCAN). This secondary analysis was designed to evaluate potential correlations between CIC-related gene expression and key clinicopathological features, including patient age, gender, and tumor stage at diagnosis.

GO and KEGG pathway analysis of CIC-related genes

To gain a comprehensive understanding of the biological roles and molecular pathways associated with CIC-related genes, Gene Ontology (GO) and Kyoto Encyclopedia of Genes and Genomes (KEGG) enrichment analyses were performed. CIC-associated gene expression profiles were retrieved from the LinkedOmics database, an online analytical platform based on TCGA datasets. GO enrichment was carried out using the DAVID (Database for Annotation, Visualization and Integrated Discovery) tool to categorize genes according to their involvement in biological processes, cellular components, and molecular functions. KEGG pathway analysis was subsequently employed to identify signaling networks and cellular mechanisms implicated in tumorigenesis, metastasis, and other CIC-associated oncogenic processes [26].

Immunohistochemistry

Paraffin-embedded tissue specimens were sectioned at 3 μm thickness, deparaffinized, and rehydrated through a graded ethanol series. Antigen retrieval was performed by boiling sections in EDTA buffer (pH 8.0) under high pressure for 15 minutes. Endogenous peroxidase activity was blocked using 0.3% hydrogen peroxide. After blocking with 5% bovine serum albumin for 45 minutes, sections were incubated with primary antibodies against EZR (Proteintech, GB111200), FAT1 (Proteintech, 17617-1-AP, 1:1000), and TP53 (Servicebio, GB112444-50), followed by application of the appropriate secondary antibody. Immunoreactivity was visualized using diaminobenzidine (DAB), and nuclei were counterstained with hematoxylin [27].

Histopathological examination

Tissue sections were stained with hematoxylin and eosin (H&E) and examined under a light microscope. Apoptosis was evaluated using TUNEL (terminal deoxynucleotidyl transferase dUTP nick-end labeling) assay and immunohistochemical staining for cleaved caspase-3. Immunofluorescence images were acquired using an inverted fluorescence microscope [27].

Cell culture

The NK-92 and Cal27 cell lines were sourced from Procell. NK-92 cells were cultured in α-MEM supplemented with 12.5% fetal bovine serum (FBS) and 12.5% horse serum, while Cal27 cells were maintained in Dulbecco's modified Eagle medium (DMEM) under standard culture conditions (37°C, 5% CO_2, humidified atmosphere). Chemotherapeutic agents were dissolved in dimethyl sulfoxide (DMSO) and directly added to the culture medium, maintaining a final DMSO concentration below 0.2%. Control groups were treated with DMSO alone. For co-culture assays, NK-92 cells were pre-labeled with CD45-PE antibody in PBS containing 1% FBS for 15 minutes. Cal27 cells were seeded into 6-well plates and cultured overnight, followed by staining with CMFDA cell tracker (Thermo Fisher Scientific) for 20 minutes. Labeled NK-92 and Cal27 cells were co-cultured for 4 hours, followed by PBS washing and detachment using trypsin/EDTA for further analysis.

Table 1. General information about the sample

No.	Blood Type	Surgery Date	Age	Primary Diagnosis	Clinical Stage	Height (cm)	Weight (kg)	Chemotherapy Regimen	No. of Cycles	End of Treatment	SCCA	Prognosis	Sex	Comorbidities	Differentiation
1	A	Jan 7, 2024	56	Tongue cancer	cT3N1M0	172	73	None	0	11 months	Positive	No recurrence	Male	None	Moderate
2	B	Apr 23, 2024	64	Buccal cancer	cT3N0M0	168	65	None	0	7 months	Negative	No recurrence	Female	Hypertension	Well
3	O	Mar 20, 2024	55	Floor-of-mouth cancer	cT4N2M0	175	74	None	0	8 months	Positive	No recurrence	Male	None	Poor
4	AB	Apr 16, 2024	49	Tongue cancer	cT3N1M0	164	69	None	0	7 months	Positive	No recurrence	Female	None	Moderate
5	B	Mar 19, 2024	64	Tongue cancer	cT3N0M0	170	70	None	0	9 months	Negative	No recurrence	Male	Hypertension, Diabetes	Poor
6	A	Apr 26, 2024	36	Tongue cancer	cT4N0M0	173	77	None	0	7 months	Positive	No recurrence	Male	None	Poor

Abbreviations: SCCA, squamous cell carcinoma antigen; cTNM, clinical tumor-node-metastasis classification; cT3N1M0 = clinical stage T3, N1, M0; cT3N0M0 = clinical stage T3, N0, M0; cT4N2M0 = clinical stage T4, N2, M0; cT4N0M0 = clinical stage T4, N0, M0.

LncRNA MIR31HG knockdown cell lines

Short hairpin RNA (shRNA) plasmids targeting the lncRNA MIR31HG, along with a pLKO.1 empty control vector, were sourced from GenePharma (Shanghai, China). For lentiviral packaging, 293FT cells were transfected with either pLKO. 1-shKCNQ1OT1 or control shRNA constructs using Lipofectamine 2000 (Invitrogen), following the manufacturer's protocol. Subsequently, CAL27 cells were transduced with lentiviral particles carrying the respective constructs, and stably transduced cell lines were selected using 2 μg/ml puromycin for 10 days.

Fluorescence microscopy for cell localization

Calcein AM and Calcein Red-Orange AM dyes were dissolved in PBS or DMSO at a concentration of 1 mg/mL and applied to the cells for 30 minutes. Cal27 cells were seeded on confocal microscopy slides and cultured overnight as a monolayer, followed by staining with Calcein Red-Orange AM. Pre-labeled NK-92 effector cells were then added. Cellular interactions were visualized using a laser scanning confocal microscope.

Isolation of CIC structures by flow cytometry

To isolate heterotypic CIC structures from co-cultured NK-92 and Cal27 cells, fluorescence-based flow cytometry strategy was employed. Prior to co-culture, NK-92 cells were labeled with CD45-PE antibody, and Cal27 cells were stained with CMFDA cell tracking dye. After 4 h of co-culture, cells were gently harvested using EDTA-free trypsin to minimize disruption of CIC structures. Cell suspensions were rinsed with PBS containing 1% FBS and immediately subjected to flow cytometry analysis (CytoFlex, Beckman Coulter). CIC structures were defined as double-positive events ($CD45^+/CMFDA^+$), indicative of Cal27 cells containing NK-92 cells. Gating thresholds were established using single-stained controls to accurately distinguish between CICs and single or aggregated cells.

Double-positive CIC populations were further sorted using a cell sorter equipped with 488 nm and 561 nm lasers. Isolated CICs were subsequently reseeded in complete DMEM medium and cultured under standard conditions (37°C, 5% CO_2).

Flow cytometric apoptosis assay

Apoptosis was quantitatively evaluated using a commercial Annexin V-FITC/Propidium Iodide (PI) Apoptosis Detection Kit. Cal27 cells were seeded into 6-well plates at a density of 2×10^6 cells/well and cultured for 24 hours to ensure adherence. Subsequently, the cells were treated with Fe/NV-CN (1 mg/mL, 2 mL) for 6 hours, followed by irradiation using a white LED light source at an intensity of 50 mW/cm^2 for 30 minutes. After irradiation, the cells were incubated for an additional 24 hours. Finally, cells were harvested and stained with Annexin V-FITC and PI in strict accordance with the manufacturer's protocol. The samples were analyzed by flow cytometer to quantify the extent of apoptotic cell death.

CCK-8 assay for NK cell cytotoxicity

The cytotoxic activity of natural killer (NK) cells against target cells was assessed using a CCK-8 assay in 96-well round-bottom plates. Co-culture experiments were performed at two distinct effector-to-target (E:T) ratios, 5:1 and 10:1. For each condition, 50 μL of the NK cell suspension was mixed with 50 μL of target cell suspension, yielding a final culture volume of 100 μL per well. All experiments were conducted in triplicate.

Control groups were set up as follows: Target cell control (OD_T): Target cells cultured alone in complete medium.

Effector cell control (OD_E): NK cells cultured alone in medium.

Co-culture group (OD_ET): NK cells and target cells co-cultured at the designated E:T ratios.

After incubation at 37°C with 5% CO_2 for 12 hours, 10 μL of CCK-8 solution (5 mg/mL, Dojindo Laboratories, Japan) was added to each well. Plates were gently shaken and incubated for an additional 4 hours. Absorbance at 450 nm was measured using a microplate reader (BioTek Instruments). The NK cell-mediated cytotoxicity was calculated using the following formula: Cytotoxicity (%) = [1-(ODET-ODE)/ODT] × 100%. OD_ET: absorbance of the NK-target co-culture group. OD_E: absorbance of NK cells alone (to account for NK cell metabolism). OD_T: absorbance of target cells alone (as reference for 100% viability).

CCK-8 assay for cell proliferation activity

Cells from each experimental group were enzymatically dissociated, counted, and seeded into 96-well plates at a density of 5×10^3 cells per well in 100 μL of complete medium. Each condition was tested in triplicate. At 24, 48, and 72 hours post-seeding, 10 μL of CCK-8 reagent was added to each well. The plates were incubated for 4 hours at 37°C in a humidified incubator with 5% CO_2. After incubation, absorbance at 450 nm was measured to determine cell viability.

Western blotting

Cells were lysed in radioimmunoprecipitation assay (RIPA) buffer (Beyotime, Shanghai, China) supplemented with protease inhibitors (Roche, Shanghai, China), and, if necessary, phosphatase inhibitors (Sangon Biotech, Shanghai, China). Protein concentrations were measured, and equal amounts of protein were subjected to 10% SDS-PAGE, followed by transfer onto polyvinylidene fluoride (PVDF) membranes. Membranes were blocked with 5% non-fat milk for 1 hour at room temperature and incubated overnight at 4°C with primary antibodies against PD-L1, E-cadherin, Bcl-2, and GAPDH (all from Abcam, USA). After washing, membranes were incubated with HRP-conjugated anti-rabbit secondary antibodies (1:5000, SA00001-2, Proteintech) for 1 hour at room temperature. Protein bands were visualized using the Tanon 5200 Multi imaging system (Tanon, Shanghai, China).

Transwell assay

To assess cell migration and invasion, CAL27 cells were harvested, washed, and resuspended in serum-free medium. For migration assays, cells were seeded into the upper chambers of Transwell inserts (Corning, USA), while invasion assays employed Matrigel-coated inserts (BD Biosciences, USA). The lower chambers were filled with medium supplemented with 10% fetal bovine serum to serve as a chemoattractant. After a 24-hour incubation at 37°C, non-migrated or non-invaded cells on the upper surface of the membrane were gently removed. Cells that migrated to the underside of the membrane were fixed in 4% paraformaldehyde and stained with 0.1% crystal violet. The number of invaded cells was quantified using a light microscope.

Scratch recovery test

For the wound healing assay, transfected CAL27 cells were cultured in complete medium until a confluent monolayer was formed. A standardized scratch was made in the monolayer, after which the detached cells were removed by washing with PBS. The cultures were maintained in serum-free medium thereafter. Images of the wound were captured at 0 and 24 hours post-scratch. Wound closure was measured using ImageJ software, and the healing rate was calculated using the formula: Wound healing rate (%) = [(area at 0 h - area at 24 h)/area at 0 h] × 100%. Each experiment was performed in triplicate.

ELISA

ELISA kits were used to measure the levels of TGF-β and IL-10 in cell culture supernatants. Standard solutions or samples (100 μL per well) were added to 96-well plates pre-coated with specific antibodies and incubated at room temperature for 2 hours. After three washes with diluted wash buffer, each well was incubated with HRP-conjugated secondary antibodies at room temperature for 1 hour. After another three washes, 100 μL of substrate solution was added to each well and incubated in the dark for 30 minutes. The reaction was terminated by adding 90 μL of stop solution per well, and absorbance was measured at 450 nm using a microplate reader. Cytokine concentrations were calculated based on a standard curve.

Colony formation

Cells were plated in 6-well plates at a density of 1,000 cells per well and incubated for 10 to 14 days to allow colony formation. Afterward, colonies were fixed, stained with crystal violet, and air-dried. Colony images were captured using a Canon Canoscan 5600F scanner (Canon, Japan).

Establishment of HNSCC xenograft mouse models

All animal experiments were approved by the Ethics Committee of Henan Cancer Hospital and conducted in accordance with institutional guidelines for animal care and use. Xenograft models were established by subcutaneously injecting 1 × 10^6 Cal27 cells into 4-week-old

male BALB/c nude mice (Charles River, China). The mice were randomly divided into three groups (n = 3 per group): Cal27 cell group, CIC group, and CIC+sh LncRNA MIR31HG group. Mice were euthanized after 7 weeks, and tumors and major organs were harvested for histopathological analysis. Tumor volumes were calculated using the formula: Volume = Length × Width^2)/2.

RNA sequencing

Total RNA was extracted from transfected CAL27 cells using TRIzol reagent (Invitrogen Life Technologies, USA) according to the manufacturer's instructions. RNA concentration and purity were assessed using a Nanodrop 2000 spectrophotometer (Thermo Fisher Scientific, USA). Libraries were constructed using the TruSeq™ RNA Sample Prep Kit (Illumina, USA) and sequenced by a certified sequencing facility. High-quality reads were aligned to the reference genome, and transcript abundance was quantified using StringTie. Differentially expressed genes were identified using the DESeq algorithm, followed by Gene Ontology (GO) and KEGG pathway enrichment analyses to uncover associated biological functions and signaling pathways.

Statistical analysis

Statistical analyses were conducted using GraphPad Prism version 8.1 (GraphPad Software, USA). Data distribution was assessed using the Shapiro-Wilk test. Variables with normal distribution are presented as mean ± standard error of the mean (SEM). Variables with non-normal distribution are presented as median with interquartile range (IQR). For comparisons between two groups, Student's t-test was used for normally distributed variables, while the Mann-Whitney U test was used for non-parametric data. For comparisons among three or more groups (e.g., Cal27, CIC, CIC + shMIR31HG), one-way ANOVA with Tukey's post hoc test was used for normally distributed variables, and Kruskal-Wallis test with Dunn's multiple comparison test for non-parametric data. For measurements collected at multiple time points (e.g., 24 h, 48 h, 72 h), repeated-measures ANOVA was used for parametric data, and Friedman test for non-parametric data, with Bonferroni correction for post hoc comparisons. A two-tailed p-value < 0.05 was considered statistically significant. All experiments were performed in biological triplicates (n = 3) unless otherwise specified.

Results

Association of CIC-related genes with HNSCC

To delineate the transcriptomic landscape of genes associated with CIC structure in HNSCC, a comparative analysis was conducted utilizing transcriptomic data from the TCGA and GTEx databases. This investigation revealed extensive transcriptional dysregulation in HNSCC tissues compared to normal controls. A heatmap of CIC-related gene expression demonstrated distinct clustering that clearly segregated tumor samples from normal samples (**Figure 1A**). Among the differentially expressed genes, MMP1, MMP12, and PLA2G7 were markedly upregulated, whereas PPP1R3C, PTN, and ANKRD20A8P were significantly downregulated. A volcano plot visualizing these changesidentified 444 upregulated and 332 downregulated genes based on stringent statistical thresholds ($|\log_2$ fold change$|$ > 0.825, P < 0.05; **Figure 1B**).

To explore the biological relevance of these gene expression alterations, we conducted pathway and ontology enrichment analyses. Gene Ontology (GO) analysis indicated that dysregulated genes were predominantly enriched in biological processes such as extracellular matrix organization, as well as in apical and basal plasma membrane components (**Figure 1C-E**), suggesting their involvement in tissue architecture and cellular polarity. KEGG pathway analysis revealed a significant downregulation of focal adhesion signaling. Concurrently, the KEGG analysis highlighted the upregulation of pathways involved in drug and cytochrome P450 metabolism and insulin signaling, while Toll-like receptor signaling pathways were suppressed (**Figure 1F**). These findings indicate a coordinated molecular shift in HNSCC, where structural and immune-related pathways are disrupted, and metabolic and pro-survival pathways are enhanced.

Collectively, these data establish that CIC-related genes are pivotal in remodeling the cellular structure, metabolic activity, and signaling

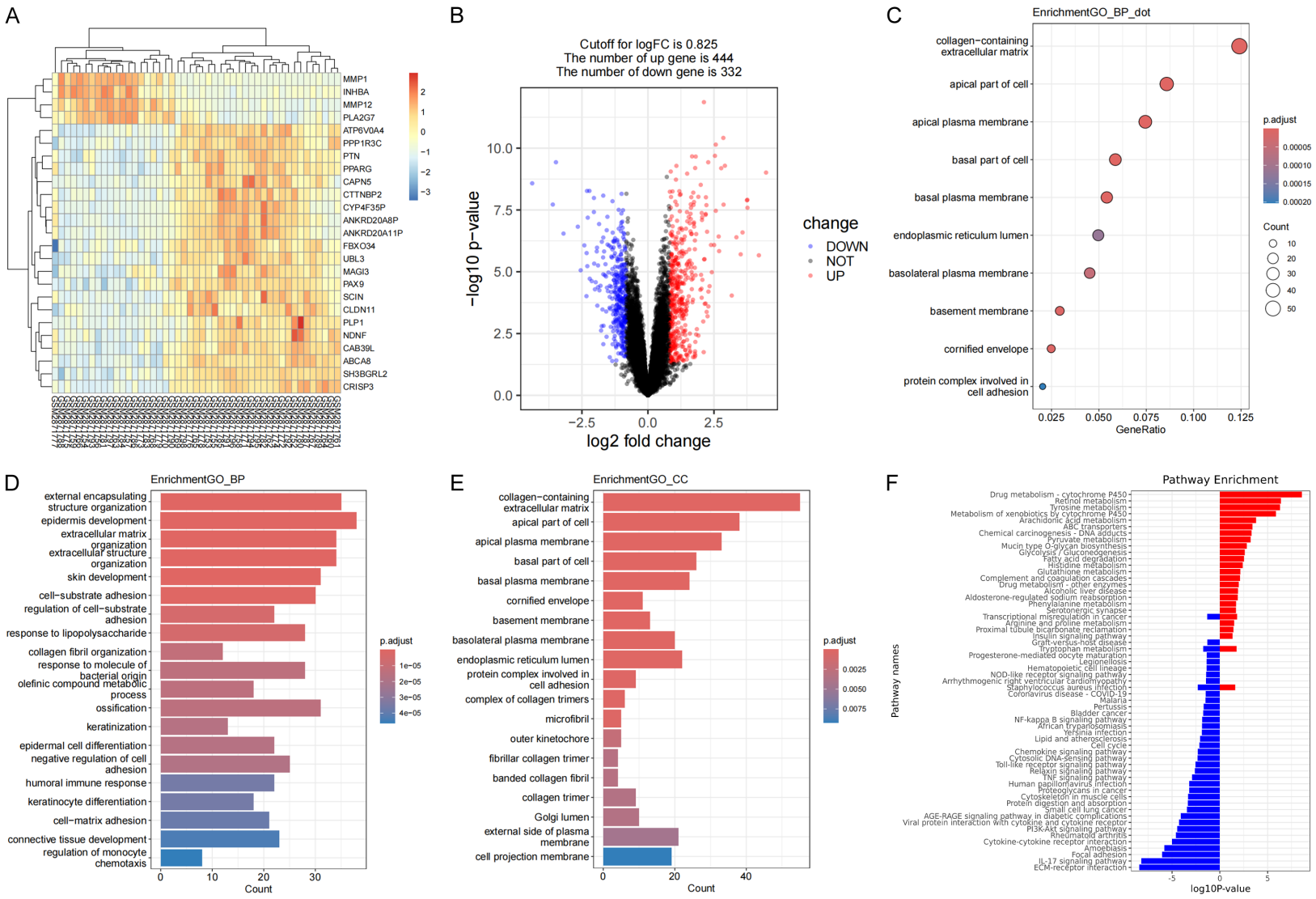

Figure 1. Differential expression and functional enrichment of CIC-related genes between normal and HNSCC tissues. A. Heatmap displaying the expression profiles of top differentially expressed capicua (CIC)-related genes. Gene expression is standardized and color-coded from low (blue) to high (red) across all samples. B. Volcano plot of DEGs. Genes with $|\log_2$ fold change$| > 0.825$ and $P < 0.05$ are considered significantly dysregulated. Red and blue dots represent significantly upregulated and downregulated genes, respectively, while gray dots denote non-significant genes. C. GO enrichment analysis for BP, presented as a bubble plot.

Representative terms include collagen-containing extracellular matrix and apical part of cell. Bubble size indicates the number of genes, and color reflects adjusted *p*-values. D. Bar plot of enriched GO biological processes. Key processes such as external encapsulating structure organization and epidermis development are significantly over-represented among DEGs. E. CC enrichment analysis highlighting components such as collagen-containing extracellular matrix, apical plasma membrane, and cell projection membrane. F. KEGG pathway enrichment analysis. Pathways are ranked by significance ($-\log_{10}$ *p*-value), with upregulated pathways shown in red and downregulated in blue. Notably enriched pathways include drug metabolism - cytochrome P450 and glycolysis/gluconeogenesis, indicating metabolic reprogramming and tumor-associated alterations. Abbreviations: CIC, capicua transcriptional repressor; HNSCC, head and neck squamous cell carcinoma; DEGs, differentially expressed genes; GO, Gene Ontology; BP, biological process; CC, cellular component; KEGG, Kyoto Encyclopedia of Genes and Genomes.

networks within HNSCC, positioning them as a compelling cluster of potential targets for therapeutic intervention.

Heterotypic CIC structures formed in HNSCC tissues and NK cells

Histological examination of HNSCC tissues revealed profound architectural disorganization consistent with malignant transformation, including cellular polymorphism and an elevated nucleus-to-cytoplasm ratio (**Figure 2A**). Immunohistochemical staining confirmed high expression of EZR, PD-L1, and TP53 in tumor regions, implicating these proteins in tumor progression (**Figure 2B**). To investigate tumor-immune cell interactions, a heterotypic CIC model was established by co-culturing Cal27 tumor cells and NK-92 cells. These CIC structures were successfully identified and quantified using flow cytometry, allowing for the isolation of CIC-positive populations (**Figure 2C**).

This model demonstrated that CIC formation conferred a significant functional advantage to the tumor cells. Compared to monocultured Cal27 cells, CIC-positive cells exhibited a marked enhancement in cell viability and a concurrent reduction in apoptosis (**Figure 2D**, **2E**). This pro-survival phenotype was substantiated at the molecular level by the upregulated anti-apoptotic protein Bcl-2 and cell adhesion molecule E-cadherin (**Figure 2J**). Furthermore, CIC-positive cells demonstrated enhanced migratory, invasive, and clonogenic potential, as evidenced by Transwell, wound healing, and colony formation assays (**Figure 2G-I**).

Crucially, CIC structures were instrumental in fostering an immunosuppressive state. Elevated secretion of immunosuppressive cytokines TGF-β and IL-10 was observed in CIC-positive cells (**Figure 2F**), alongside increased expression of the immune checkpoint protein PD-L1 (**Figure 2J**). These changes significantly impaired NK cell-mediated cytotoxicity, providing a potent mechanism for HNSCC cells to evade immune destruction (**Figure 2K**).

Heterotypic CIC structures conferred chemoresistance to Cal27 cells

To determine whether CIC structures mediate chemoresistance in HNSCC, we challenged both standalone CAL27 cells and CIC-forming cells with clinically relevant concentrations of cisplatin (2.5 μM) and gemcitabine (5 μM). The *in vitro* results demonstrated a clear divergence in drug sensitivity: while gemcitabine significantly reduced the viability of CAL27 cells over 48 to 72 hours, CIC-positive cells retained high viability under identical conditions (**Figure 3A**, **3B**). This survival advantage was mechanistically linked to the evasion of programmed cell death. Flow cytometry revealed significantly lower apoptotic rates in CIC-positive cells compared to CAL27 cells when subjected to the same therapeutic agents (**Figure 3C**). Cal27-derived tumors, indicating marked resistance to both cisplatin and gemcitabine. Specifically, CIC cells maintained tumor growth under the same treatment conditions, while Cal27 cells exhibited a significant reduction in tumor volume (**Figure 3D**).

These in vitro observations were subsequently validated in a xenograft model. Mice bearing CIC-derived tumors demonstrated substantial resistance to systemic chemotherapy. Following treatment with either cisplatin or gemcitabine, histological analysis of CAL27-derived tumors revealed extensive necrosis and a depleted population of surviving cancer cells. In contrast, CIC-derived tumors maintained structural integrity and viable tumor cell populations (**Figure 3E**). This enhanced resilience was further corroborated by PD-L1 immunohistochemistry and TUNEL assays, which showed preserved cellular morphology and reduced apoptosis in the CIC tumors (**Figure 3F**, **3G**).

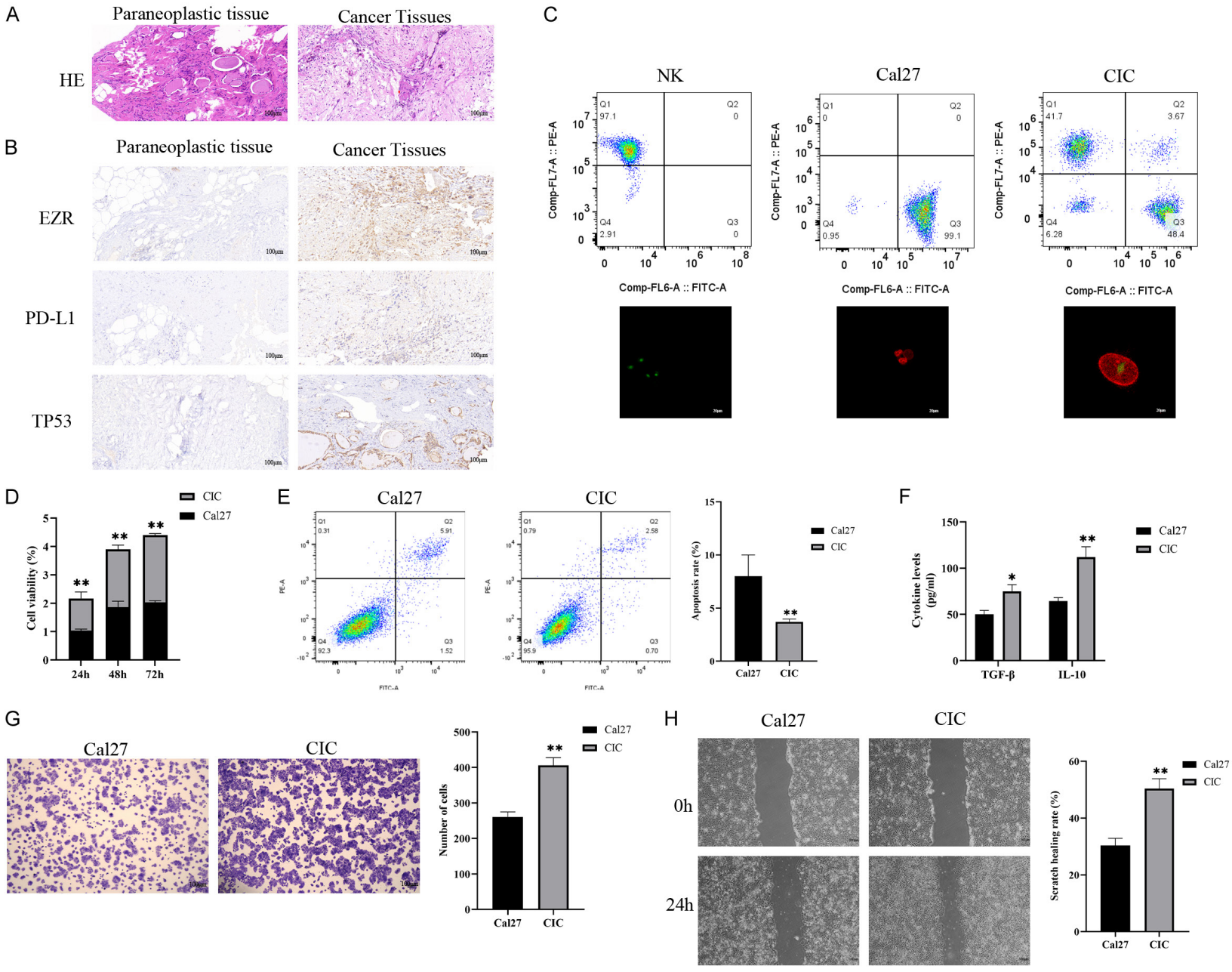
A
Paraneoplastic tissue
Cancer Tissues
HE
B
Paraneoplastic tissue
Cancer Tissues
EZR
PD-L1
TP53
C
NK
Cal27
CIC
Comp-FL7-A :: PE-A
Comp-FL6-A :: FITC-A
Q1 97.1
Q2 0
Q4 2.91
Q3 0
Q1 0
Q2 0
Q4 0.95
Q3 99.1
Q1 41.7
Q2 3.67
Q4 6.28
Q3 48.4
D
CIC
Cal27
Cell viability (%)
24h
48h
72h
E
Cal27
CIC
Q1 0.31
Q2 5.91
Q4 92.3
Q3 1.52
Q1 0.79
Q2 2.58
Q4 95.9
Q3 0.70
Apoptosis rate (%)
Cal27
CIC
F
Cytokine levels (pg/ml)
TGF-β
IL-10
Cal27
CIC
G
Cal27
CIC
Number of cells
Cal27
CIC
H
Cal27
CIC
0h
24h
Scratch healing rate (%)
Cal27
CIC

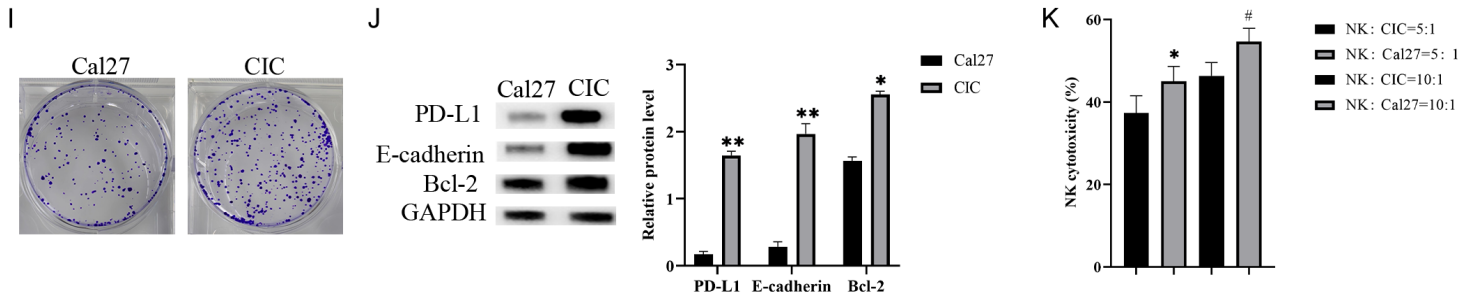

Figure 2. HNSCC and NK cells form heterogeneous CIC structures to promote cancer cell immune escape. Arrows indicate CIC structures. A. Hematoxylin and eosin (HE) staining (15×). Scale bar 100 μm. B. Immunohistochemistry of EZR, PD-L1 and TP53 in pro- and cancerous tissues (15×). Scale bar 100 μm. C. Flow cytometry analysis of NK cells, CAL27 cells and CIC cells showing different expression profiles of cell surface markers and fluorescence imaging. NK cells (green), CAL27 cells (red) (20×). Scale bar 20 μm. D. Cell viability (CCK-8 assay) of CAL27 and CIC cells at 24, 48, and 72 hours. Data are presented as mean ± SEM. Statistical analysis was performed using repeated-measures ANOVA followed by Bonferroni post hoc test. *P < 0.05, **P < 0.01, ***P < 0.001. E. Flow cytometry analysis of apoptosis of CAL27 and CIC cells showed a low apoptosis rate of CIC cells. F. Cytokine levels of TGF-β and IL-10 in CAL27 and CIC cells. Data are presented as median (IQR). Comparisons were made using Mann-Whitney U test. *P < 0.05, **P < 0.01. G. Transwell invasion assay showed that the migration ability of CIC cells was significantly enhanced compared with that of CAL27 cells (4×). Scale bar 100 μm. H. Scratch wound healing assay showed enhanced wound closure ability of CIC cells after 24 hours (4×). Scale bar 100 μm. I. Colony formation assay. J. Western blot analysis of the expression of immune checkpoint markers PD-L1, E-cadherin, Bcl-2 in CAL27 and CIC cells. K. NK cell killing. Statistical significance was defined as follows: *P < 0.05, **P < 0.01, ***P < 0.001, and ns, not significant. n = 3 biological replicates. Abbreviations: HE, hematoxylin and eosin; EZR, ezrin; PD-L1, programmed death-ligand 1; TP53, tumor protein p53; NK, natural killer cells; CCK-8, Cell Counting Kit-8; CIC, cancer-initiating cells; TGF-β, transforming growth factor beta; IL-10, interleukin-10; ELISA, enzyme-linked immunosorbent assay; E:T, effector-to-target ratio; SD, standard deviation.

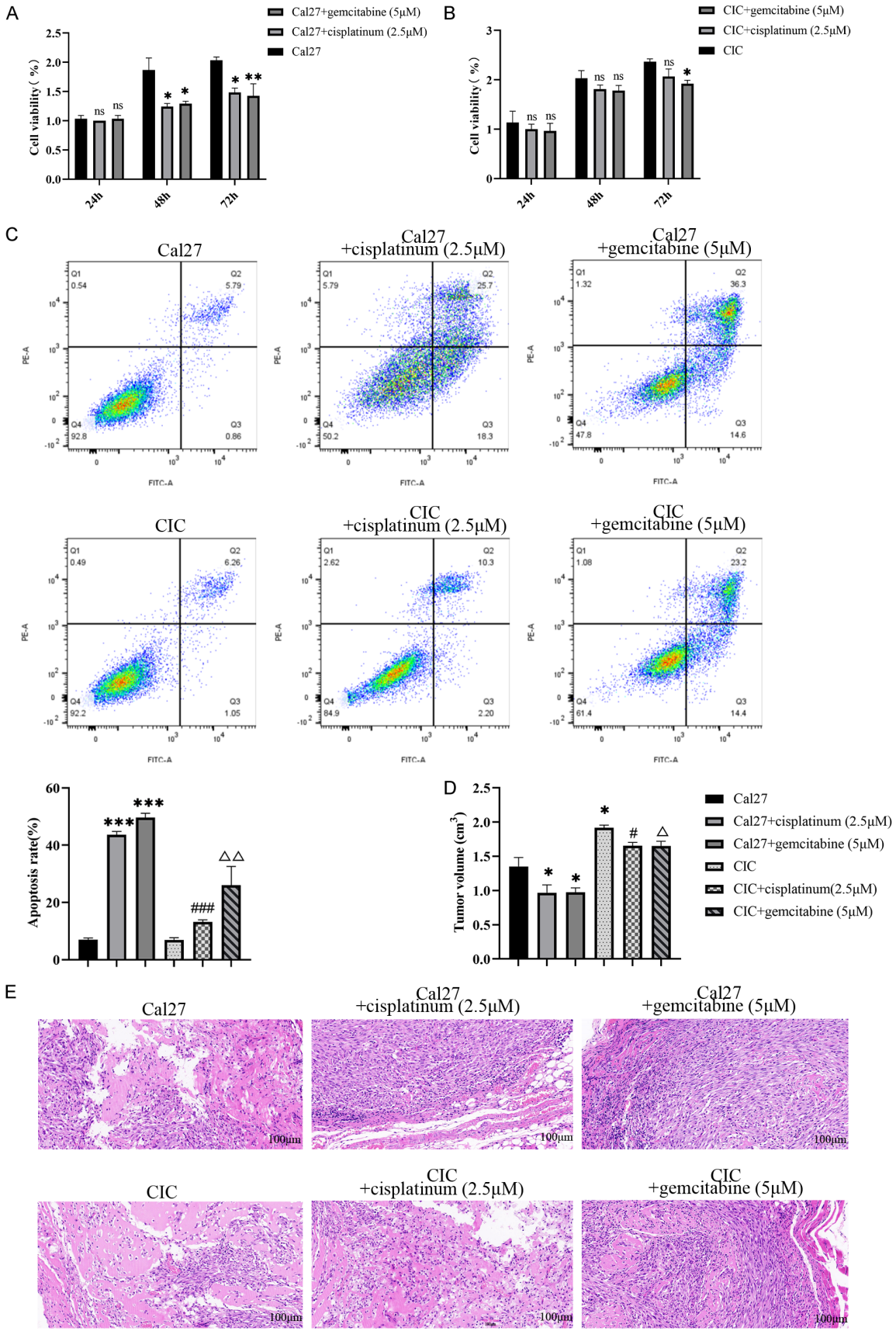
A
Cal27+gemcitabine (5μM)
Cal27+cisplatinum (2.5μM)
Cal27
Cell viability (%)
24h
48h
72h
B
CIC+gemcitabine (5μM)
CIC+cisplatinum (2.5μM)
CIC
C
Cal27
Cal27 +cisplatinum (2.5μM)
Cal27 +gemcitabine (5μM)
CIC
CIC +cisplatinum (2.5μM)
CIC +gemcitabine (5μM)
PE-A
FITC-A
Apoptosis rate(%)
D
Tumor volume (cm3)
Cal27
Cal27+cisplatinum (2.5μM)
Cal27+gemcitabine (5μM)
CIC
CIC+cisplatinum(2.5μM)
CIC+gemcitabine (5μM)
E
100μm

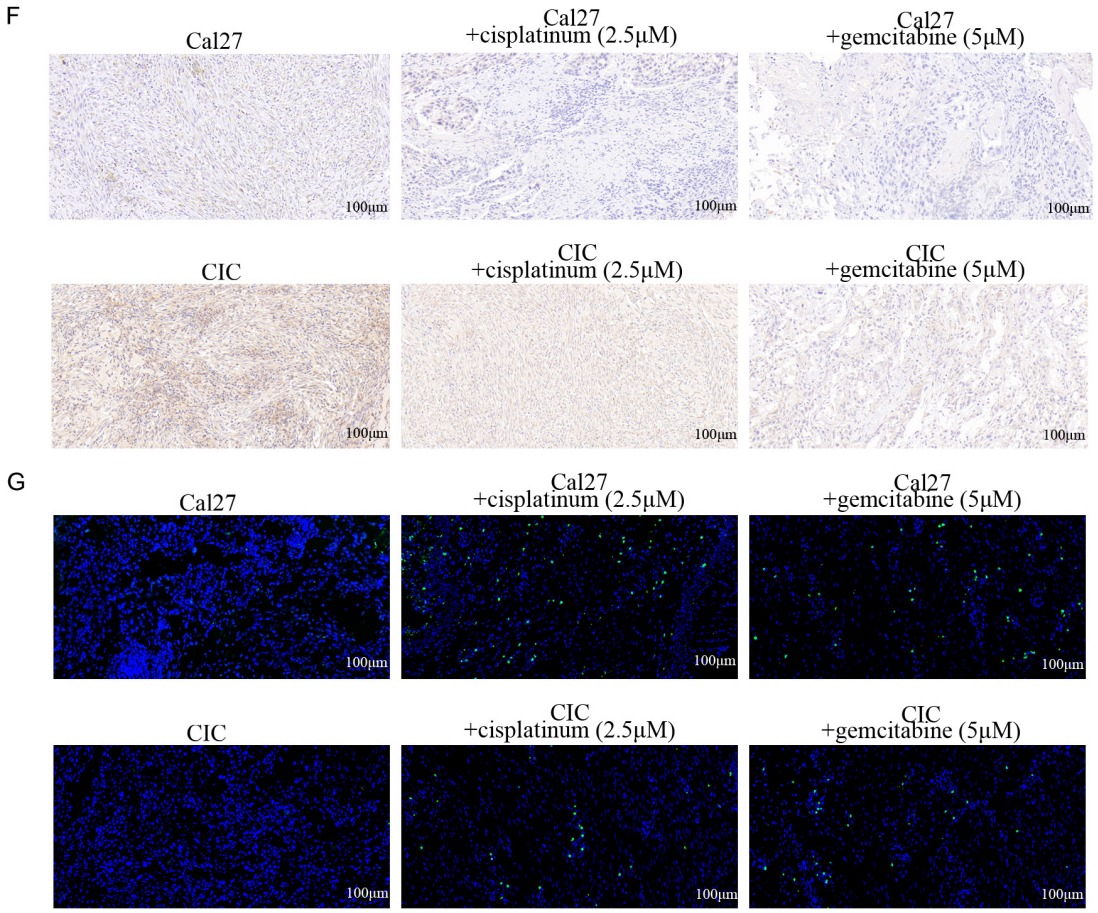

Figure 3. CIC structures resist the effect of chemotherapeutic agents on Cal. A. Cell survival of CAL27 cells treated with cisplatin or gemcitabine for 24, 48 and 72 hours. Statistical significance was defined as follows: Compared with Cal27, *P < 0.05, **P < 0.01, and ns, not significant. n = 3 biological replicates. B. Cell survival of CIC cells treated with cisplatin or gemcitabine for 24, 48 and 72 hours. Statistical significance was defined as follows: Compared with CIC, *P < 0.05, and ns, not significant. n = 3 biological replicates. C. Flow cytometry analysis of apoptosis in Cal27 and CIC cells treated with cisplatin or gemcitabine. Data are expressed as median (IQR) and analyzed using Kruskal-Wallis test followed by Dunn's post hoc test. Statistical significance was defined as follows: Compared with Cal27, ***P < 0.001; compared with Cal27+cisplatinum (2.5 μM), #P < 0.05, ###P < 0.001; compared with CIC+gemcitabine (5 μM), $^{\Delta\Delta}$P < 0.001. n = 3 biological replicates. D. Tumor invasion assay. Statistical significance was defined as follows: Compared with Cal27, *P < 0.05; compared with Cal27+cisplatinum (2.5 μM), #P < 0.05; compared with CIC+gemcitabine (5 μM), $^{\Delta}$P < 0.05. n = 3 biological replicates. E. HE staining of CAL27 and CIC cells treated with cisplatin or gemcitabine. Arrows indicate CIC structures (15×). Scale bar 100 μm. F. Immunohistochemical analysis of apoptosis markers in cisplatin- or gemcitabine-treated CAL27 and CIC cells (15×). Scale bar 100 μm. G. Tunel detection of apoptosis in transplanted tumor tissues (15×). Scale bar 100 μm. Statistical significance was defined as follows: *P < 0.05, **P < 0.01, ***P < 0.001, and ns, not significant. n = 3 biological replicates. Abbreviations: CIC, cancer-initiating cell; CAL27, parental human tongue squamous cell carcinoma cell line; HE, hematoxylin and eosin; TUNEL, terminal deoxynucleotidyl transferase dUTP nick end labeling; SD, standard deviation; CCK-8, Cell Counting Kit-8.

Collectively, these findings provide compelling evidence that the formation of CIC structures confers profound chemoresistance both in vitro and in vivo.

Transcriptomic analysis identified MIR31HG as a key lncRNA in CIC-positive HNSCC cells

To uncover lncRNA-mediated regulatory mechanisms potentially driving CIC formation and immune escape in HNSCC, we performed transcriptome-wide RNA sequencing on CIC-positive (Group A) and CIC-negative (Group B) Cal27 cells, which were sorted based on heterotypic CIC formation via flow cytometry as described earlier. This analysis aimed to identify differentially expressed lncRNAs associated with the aggressive phenotype conferred by CIC structures. Global transcriptomic profiling

revealed a substantial upregulation of lncRNA expression in CIC-positive cells (**Figure 4A-C**). Hierarchical clustering based on RPKM values distinctly separated CIC^+ and CIC^- groups, indicating a unique lncRNA expression signature associated with CIC phenotype (**Figure 4D**, **4E**). Among the dysregulated lncRNAs, MIR31HG emerged as one of the most significantly upregulated transcripts in CIC-positive cells, suggesting its potential role in mediating CIC-associated tumor behaviors. To explore the functional implications of these differentially expressed lncRNAs, we performed GO and KEGG enrichment analyses on their predicted cis- and trans-target genes. Cis-targets were significantly enriched in pathways involved in cellular structure organization and biological regulation (**Figure 4F**), whereas KEGG analysis revealed prominent enrichment in immune-regulatory and oncogenic pathways, such as PI3K-Akt signaling and cell adhesion (**Figure 4G**). Trans-target analysis further implicated pathways related to external stimuli response and immune modulation, reinforcing the hypothesis that these lncRNAs - including MIR31HG - may act as upstream regulators of tumor-immune interactions (**Figure 4H**, **4I**).

These findings prompted us to investigate the functional role of MIR31HG in detail. As one of the top differentially expressed lncRNAs in CIC-positive cells and previously implicated in HNSCC and other cancers, MIR31HG was selected for downstream functional validation.

LncRNA MIR31HG promoted heterogeneous CIC in HNSCC

To determine the functional role of lncRNA MIR31HG in maintaining the aggressive phenotype of CIC structures, we performed targeted knockdown using shRNA. Silencing of MIR31HG resulted in a striking disruption of CIC integrity, as evidenced by the loss of co-localization between NK cells and Cal27 cells in fluorescence microscopy (**Figure 5A**). This structural collapse was accompanied by a profound reversal of malignant cellular behaviors. Specifically, MIR31HG depletion significantly reduced cell viability, migration and invasion, and increased apoptosis (**Figure 5B-E**). Furthermore, MIR31HG knockdown effectively disrupted the immunosuppressive properties of CIC structures. Levels of inhibitory cytokines TGF-β and IL-10 were sharply reduced (**Figure 5G**). At the molecular level, Western blot analysis confirmed that MIR31HG knockdown significantly downregulated the expression of immune checkpoint protein PD-L1 and adhesion molecule E-cadherin, consistent with the observed functional changes (**Figure 5F**). Notably, although Bcl-2 expression levels are elevated in CIC-positive cells, silencing lncRNA MIR31HG weakens the anti-apoptotic effect of the CIC structure, potentially making these cells more susceptible to apoptosis.Crucially, MIR31HG knockdown restored chemosensitivity. CIC-positive cells with MIR31HG knockdown became highly susceptible to both cisplatin and gemcitabine, exhibiting dramatically decreased cell viability and significantly increased drug-induced apoptosis (**Figure 5H**, **5I**). These findings identify MIR31HG as a key mediator of CIC formation, immune escape, and chemoresistance in HNSCC.

Effects of lncRNA MIR31HG silencing on CIC xenograft tumors

To validate the pivotal role of MIR31HG in vivo, we evaluated its impact on tumor progression in a xenograft model. Silencing of lncRNA MIR31HG in CIC-positive cells profoundly attenuated their tumorigenic potential. Tumors derived from CIC+sh LncRNA MIR31HG cells exhibited a significant reduction in volume compared to the control group, confirming the essential role of MIR31HG in sustaining tumorigenicity (**Figure 6A**). H&E staining revealed that tumors from the MIR31HG knockdown group displayed reduced cellular density and disorganized tissue architecture, consistent with a less aggressive tumor phenotype (**Figure 6B**). Immunohistochemical staining for PD-L1 shows higher expression in CIC cells compared to Cal27 cells, with a noticeable reduction in PD-L1 expression in CIC+sh LncRNA MIR31HG cells (**Figure 6C**). These morphological changes were directly correlated with a surge in apoptotic cell numbers in the tumors from MIR31HG knockdown group (**Figure 6D**). These in vivo results conclusively demonstrate that targeting MIR31HG impairs HNSCC tumor growth by promoting apoptosis.

Discussion

Cell-in-cell (CIC) structures are characterized by the complete internalization of one or more viable cells within another, a phenomenon that

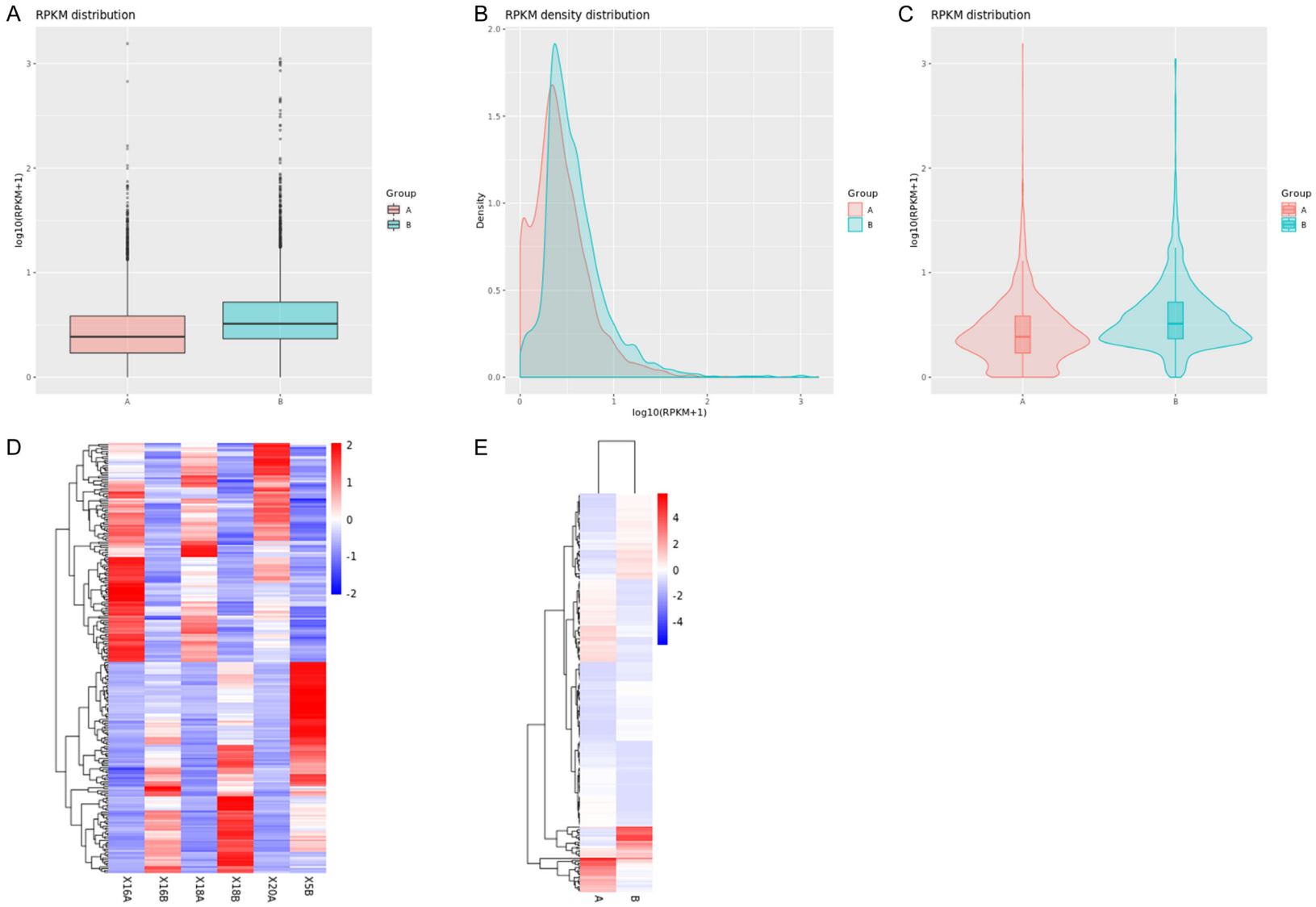
A
RPKM distribution
log10(RPKM+1)
Group
A
B
B
RPKM density distribution
Density
log10(RPKM+1)
C
RPKM distribution
D
X16A
X16B
X18A
X18B
X20A
X5B
E

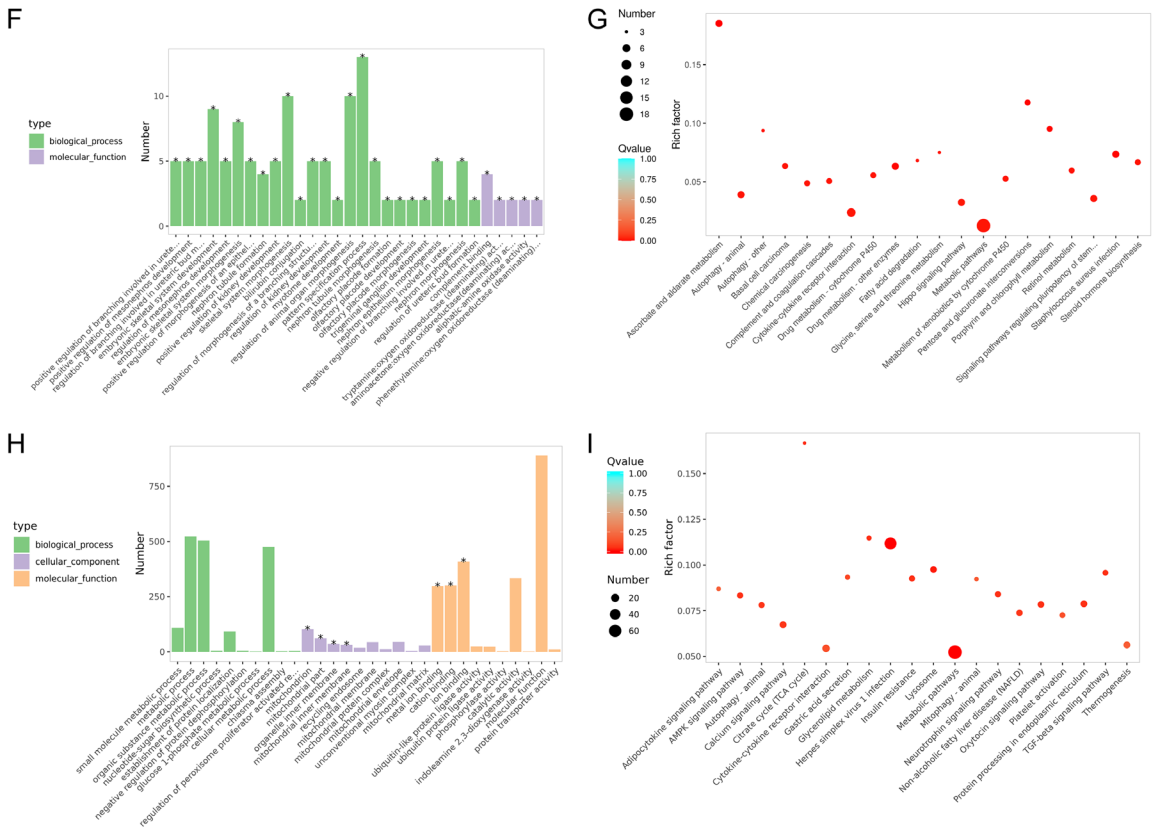

Figure 4. LncRNA expression differences and analysis. A. Boxplot showing the distribution of RPKM values for lncRNAs in Group A and Group B, indicating differential expression between the groups. B. RPKM density distribution of log-transformed values across the two groups, showing higher expression levels in Group A. C. Violin plot of RPKM distribution for lncRNAs in Group A and Group B, confirming expression differences between the two conditions. D. Heatmap of lncRNA expression levels across different samples, with hierarchical clustering revealing differential expression between the groups. E. Hierarchical clustering of lncRNAs based on expression profiles, supporting differential regulation between the groups. F. GO enrichment analysis of cis-target genes associated with lncRNAs revealed significant enrichment in processes related to biological regulation and cellular component organization. G. Kyoto Encyclopedia of Genes and Genomes (KEGG) pathway enrichment analysis of cis-target genes highlighted pathways involved in cancer progression and immune regulation. H. GO enrichment analysis of trans-target genes of lncRNAs demonstrated their involvement in signal transduction and responses to various stimuli. I. KEGG pathway analysis for trans-target genes, identifying pathways related to neurodegenerative diseases and immune response. Abbreviations: lncRNA, long non-coding RNA; RPKM, reads per kilobase per million mapped reads; GO, Gene Ontology; KEGG, Kyoto Encyclopedia of Genes and Genomes; cis-target, genes located proximal to lncRNAs; trans-target, genes regulated by lncRNAs through distant mechanisms.

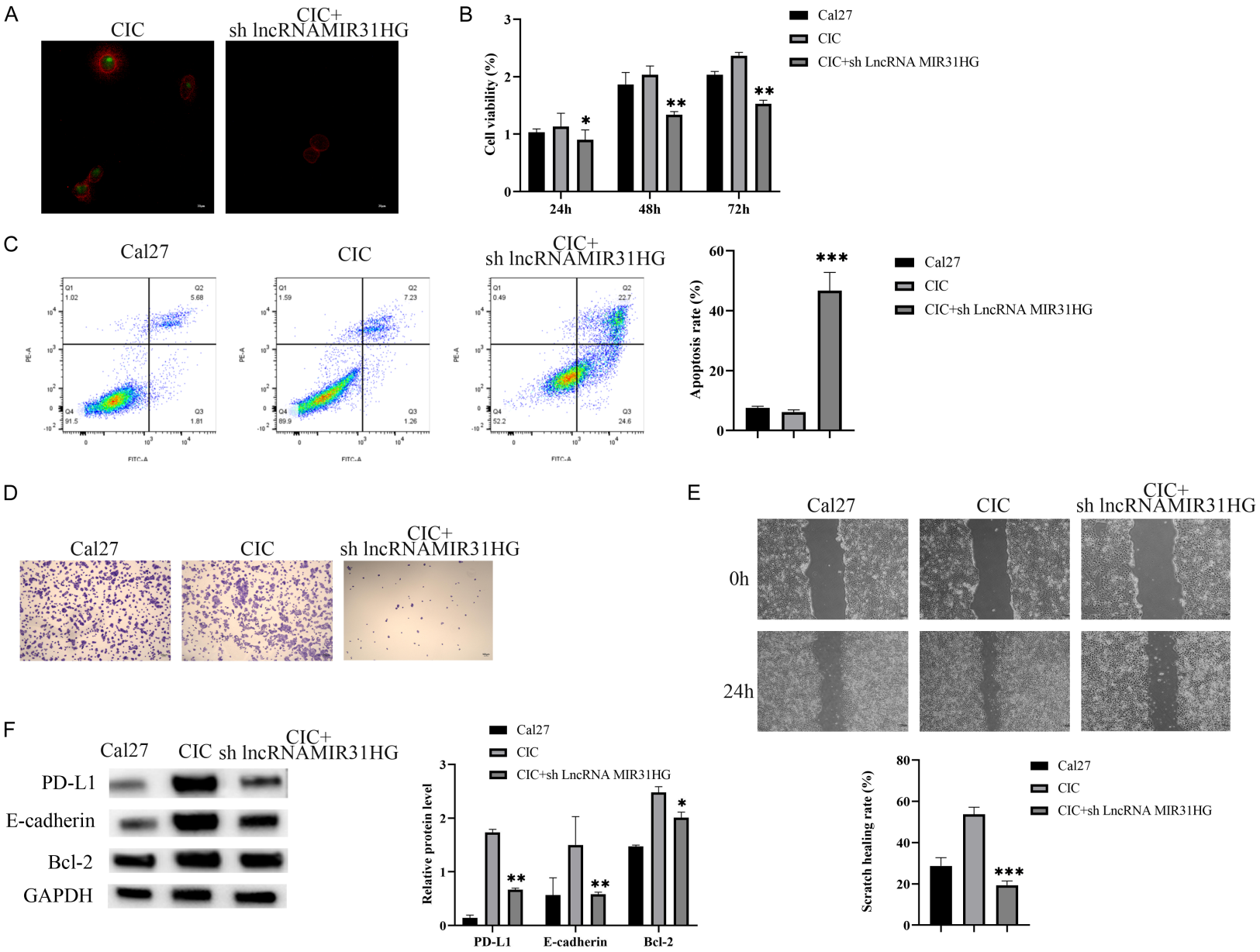
A
CIC
CIC+
sh lncRNAMIR31HG
B
Cal27
CIC
CIC+sh LncRNA MIR31HG
Cell viability (%)
24h
48h
72h
C
Cal27
CIC
CIC+
sh lncRNAMIR31HG
Apoptosis rate (%)
D
Cal27
CIC
CIC+
sh lncRNAMIR31HG
E
Cal27
CIC
CIC+
sh lncRNAMIR31HG
0h
24h
Scratch healing rate (%)
F
Cal27
CIC
CIC+
sh lncRNAMIR31HG
PD-L1
E-cadherin
Bcl-2
GAPDH
Relative protein level

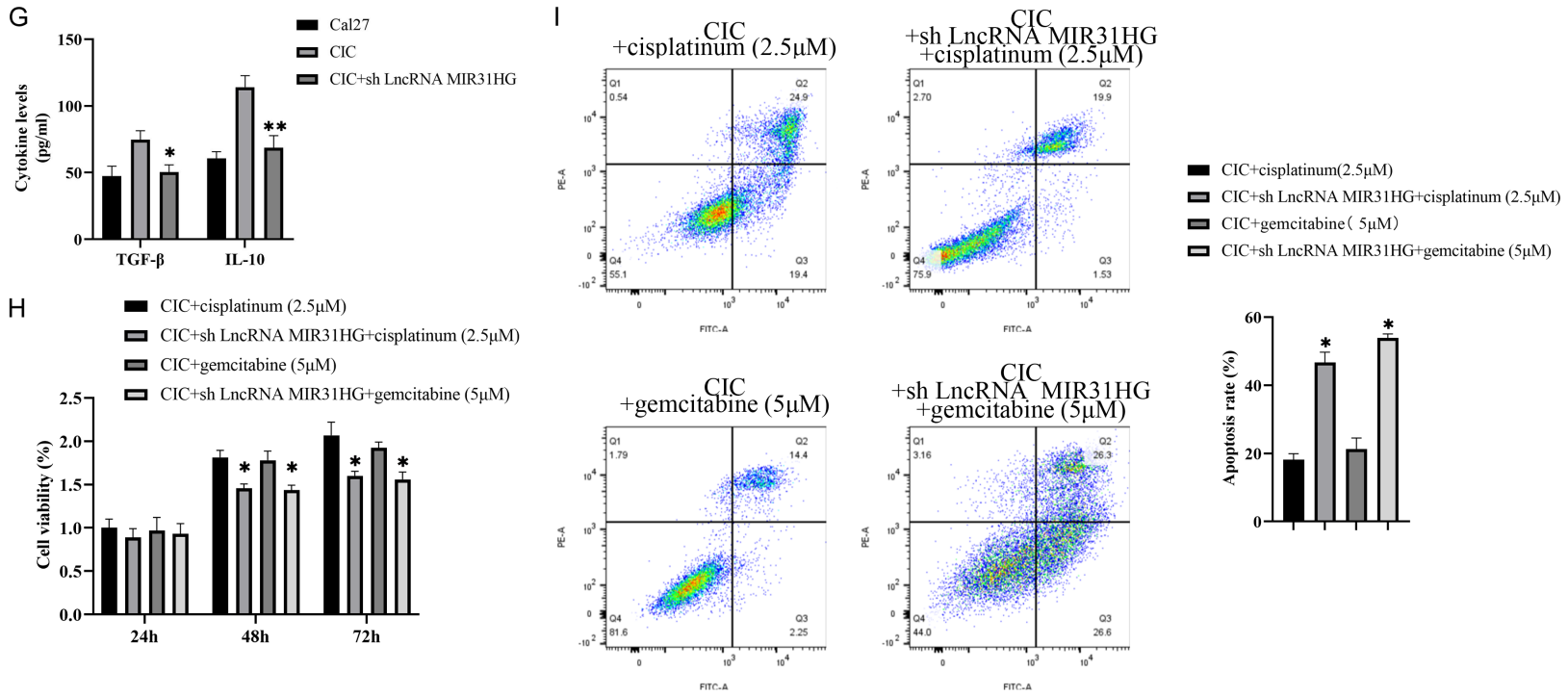

Figure 5. Effects of lncRNA MIR31HG silencing on CIC structure and cellular behavior. A. Fluorescence microscopy images showing reduced co-localization of NK and CAL27 cells in CIC cells upon silencing of lncRNA MIR31HG (20×). Scale bar 20 μm. B. Cell viability assay showing significant reduction in cell viability of CIC cells with silenced lncRNA MIR31HG compared to control at 48 and 72 hours. C. Flow cytometry analysis of apoptosis in CAL27, CIC, and CIC+sh LncRNA MIR31HG cells, showing increased apoptosis in CIC+sh LncRNA MIR31HG cells. D. Transwell migration assay showing reduced migration of CIC+sh LncRNA MIR31HG cells compared to control CIC cells (4×). Scale bar 100 μm. E. Wound healing assay showing reduced wound closure in CIC+sh LncRNA MIR31HG cells compared to control CIC cells (4×). Scale bar 100 μm. F. Western blot analysis showing decreased expression of immune checkpoint proteins PD-L1, E-cadherin, Bcl-2 in CIC+sh LncRNA MIR31HG cells compared to control. G. Cytokine secretion (TGF-β and IL-10) in supernatants from CIC+sh LncRNA MIR31HG cells and control CIC cells, showing reduced cytokine levels in silenced cells. H. Cell viability analysis of CIC+sh LncRNA MIR31HG cells treated with cisplatin or gemcitabine, showing reduced resistance to chemotherapy. I. Flow cytometry analysis of apoptosis in CIC+sh LncRNA MIR31HG cells treated with cisplatin or gemcitabine, showing significantly increased apoptosis in silenced cells. Statistical significance was defined as follows: *P < 0.05, **P < 0.01, ***P < 0.001, and ns, not significant. n = 3 biological replicates. Abbreviations: lncRNA, long non-coding RNA; MIR31HG, MIR31 host gene; CIC, cancer-initiating cell; NK, natural killer cell; PD-L1, programmed death-ligand 1; Bcl-2, B-cell lymphoma 2; TGF-β, transforming growth factor beta; IL-10, interleukin 10; CCK-8, Cell Counting Kit-8; ELISA, enzyme-linked immunosorbent assay.

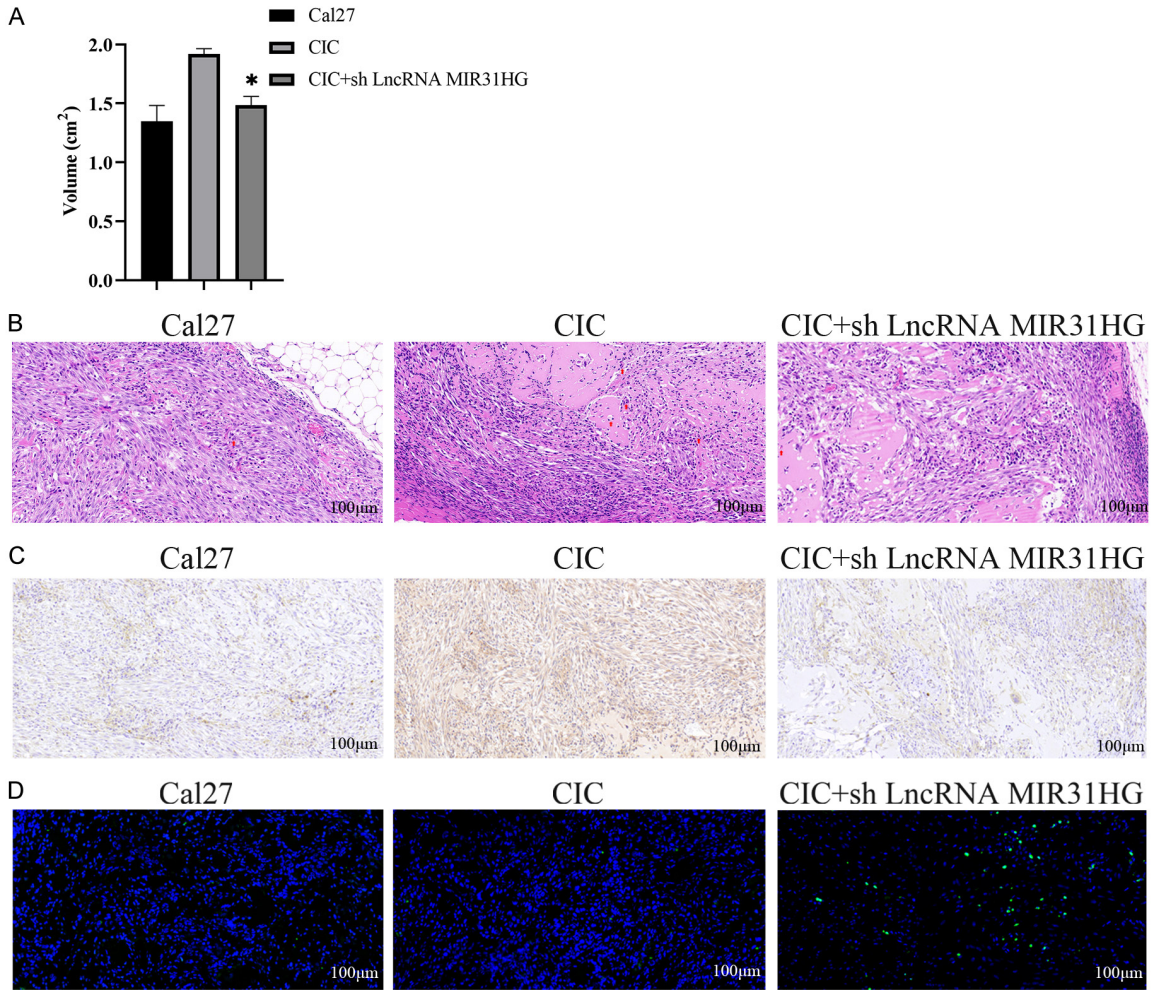

Figure 6. Effects of lncRNA MIR31HG Silencing on CIC Xenograft Tumors. A. Tumor volume comparison among CAL27, CIC, and CIC + shMIR31HG xenograft groups. Data are shown as mean ± SEM, and analyzed using one-way ANOVA with Tukey's multiple comparison test. **P < 0.01, ***P < 0.001. B. HE staining of tumor sections from CAL27, CIC, and CIC+sh LncRNA MIR31HG groups, indicating altered tumor morphology and reduced cellular density in the silenced group (15×). Scale bar 100 μm. C. Immunohistochemical analysis of PD-L1 expression in tumor sections from CAL27, CIC, and CIC+sh LncRNA MIR31HG groups, showing reduced PD-L1 expression in CIC+sh lncRNA MIR31HG tumors (15×). Scale bar 100 μm. D. Fluorescence images showing increased apoptosis in CIC+sh LncRNA MIR31HG cells compared to control CIC cells, with green fluorescence indicating apoptotic cells (15×). Scale bar 100 μm. Statistical significance was defined as follows: *P < 0.05, **P < 0.01, ***P < 0.001, and ns, not significant. n = 3 biological replicates. Abbreviations: lncRNA, long non-coding RNA; MIR31HG, MIR31 host gene; CIC, cancer-initiating cell; HE, hematoxylin and eosin; PD-L1, programmed death-ligand 1; TUNEL, terminal deoxynucleotidyl transferase dUTP nick end labeling; DAPI, 4', 6-diamidino-2-phenylindole; SD, standard deviation.

often culminates in the degradation of the engulfed cell [12]. The formation of these structures is a dynamic process orchestrated by key molecular components, including adherens junctions and myosin-driven contractile rings [28]. This unique form of cell-cell interaction was first observed in tumors by Steinhaus in 1891, and later described in more detail by H. Stroebe, who coined the term "cell cannibalism" due to its morphological resemblance to phagocytosis [29]. CIC structures are a prevalent feature in diverse human malignancies and are broadly categorized into two types: homotypic CICs, where tumor cells engulf other tumor cells, and heterotypic CICs, where tumor cells internalize immune effector cells [30].

Within the tumor microenvironment (TME), the formation of heterotypic CICs represents a crucial adaptive strategy employed by cancer cells to overcome metabolic challenges [31]. Under conditions of nutrient deprivation, such as lim-

ited glucose or amino acids, tumor cells internalize neighboring cells to utilize their catabolic products as alternative metabolic substrates [32, 33]. This behavior provides a distinct survival advantage, sustaining proliferation and metastatic potential even in a hostile metabolic landscape or under therapeutic pressure. Consequently, heterotypic CIC formation is increasingly recognized not only as a potent mechanism of immune evasion but also as a significant driver of tumor progression, with potential implications as a potential prognostic marker [34].

A primary consequence of CIC formation is the direct subversion of anti-tumor immunity. Cytotoxic effectors, notably NK cells and $CD8^+$ T lymphocytes, are susceptible to engulfment and subsequent intracellular degradation by tumor cells, facilitating immune escape [35-37]. In vitro studies have shown that following co-culture with activated T cells, the surviving populations of human breast, colon, and melanoma tumor cells are selectively enriched in CIC structures, while their non-engulfing counterparts are largely eliminated [11]. This observation is corroborated by clinical observations of high CIC frequencies in recurrent melanomas following T-cell infiltration therapy. Furthermore, tumor cells with formed CICs exhibit enhanced resistance to both cytotoxic agents and NK cell-mediated lysis [37]. The molecular and cellular determinants that confer this differential susceptibility, however, remain incompletely understood.

CIC formation is orchestrated by a complex regulatory network involving genes that regulate cytoskeletal architecture, vesicle trafficking, and cell adhesion [38]. Among these, Ezrin, a key member of the ezrin-radixin-moesin (ERM) protein family, functions as a pivotal regulator. Ezrin functions as a linker between the plasma membrane and the actin cytoskeleton, regulating cell morphology, motility, and signal transduction in epithelial cells [39, 40]. Specifically, its interaction with Caveolin-1 facilitates cytoskeleton remodeling required for vacuole formation during homotypic CIC development [41].

In this study, we sought to define the role of CIC structure in HNSCC progression. Analysis of clinical HNSCC specimens revealed that the expression of CIC-associated proteins EZR and TP53 was significantly elevated in tumor tissues, indicating a heightened predisposition toward CIC formation. Complementary in vitro experiments using CAL27 cells confirmed that CIC formation promotes aggressive cellular phenotypes, which aligns with previous reports suggesting that CICs can fuel tumor progression by enhancing growth and metastasis.

To elucidate the mechanisms underlying therapeutic resistance in HNSCC, we established a clinically relevant co-culture model using HNSCC-representative CAL27 cells and NK-92 cells, a standardized effector model for evaluating NK cell cytotoxicity [42]. This system allowed us to probe tumor-immune interactions, with a particular focus on the role of lncRNA MIR31HG. Our key finding is that the formation of CICs within this model confers a dual-resistance phenotype. These structures fostered significant immune evasion, evidenced by increased CAL27 cell survival and marked upregulation of the immune checkpoint protein PD-L1, thereby reducing susceptibility to NK cell-mediated cytotoxicity. Concurrently, the CIC structures demonstrated marked chemoresistance, maintaining viability following treatment with cisplatin and gemcitabine. This dual capacity to simultaneously evade immune surveillance and withstand chemotherapy underscores CIC structures as critical contributors to treatment failure in HNSCC.

Building on this, our investigation identified lncRNA MIR31HG as a key molecular driver of this process. We discovered that MIR31HG knockdown disrupted CIC formation and significantly attenuated the associated malignant behaviors. These findings position MIR31HG as a critical upstream orchestrator of CIC structural formation and a functional modulator of their pro-tumorigenic behavior.

In conclusion, this study delineates a critical mechanism of tumor progression in HNSCC, demonstrating that the formation of CIC structures drives malignancy by conferring dual resistance to both immune surveillance and conventional chemotherapy. LncRNA MIR31HG serves as a key upstream regulator of CIC formation and function, providing a crucial molecular entry point for therapeutic intervention. Future strategies aimed at disrupting the MIR31HG-CIC regulatory axis hold the potential to dismantle this formidable tumor defense mechanism, thereby resensitizing HNSCC to

existing treatments and providing a solid theoretical foundation for novel combination immunotherapies.

Acknowledgements

This work was supported by Henan provincial Medical Science and Technology Research Project (No. LHGJ20220196); and Project of Science and Technology in Science and Technology Department of Henan Province (No. 232102310285).

Disclosure of conflict of interest

None.

Address correspondence to: Lisong Lin, Department of Oral and Maxillofacial Surgery, School and Hospital of Stomatology, Fujian Medical University, No. 246, Yangqiao Middle Road, Gulou District, Fuzhou 35000, Fujian, P. R. China. E-mail: linlisong2025@126.com

References

[1] Gong Y, Bao L, Xu T, Yi X, Chen J, Wang S, Pan Z, Huang P and Ge M. The tumor ecosystem in head and neck squamous cell carcinoma and advances in ecotherapy. Mol Cancer 2023; 22: 68.

[2] Cillo AR, Kürten CHL, Tabib T, Qi Z, Onkar S, Wang T, Liu A, Duvvuri U, Kim S, Soose RJ, Oesterreich S, Chen W, Lafyatis R, Bruno TC, Ferris RL and Vignali DAA. Immune landscape of viral- and carcinogen-driven head and neck cancer. Immunity 2020; 52: 183-199, e9.

[3] Ghosh S, Shah PA and Johnson FM. Novel systemic treatment modalities including immunotherapy and molecular targeted therapy for recurrent and metastatic head and neck squamous cell carcinoma. Int J Mol Sci 2022; 23: 7889.

[4] Chen Y, Zhong NN, Cao LM, Liu B and Bu LL. Surgical margins in head and neck squamous cell carcinoma: a narrative review. Int J Surg 2024; 110: 3680-3700.

[5] Bridges MC, Daulagala AC and Kourtidis A. LNCcation: lncRNA localization and function. J Cell Biol 2021; 220: e202009045.

[6] Zhang Y. LncRNA-encoded peptides in cancer. J Hematol Oncol 2024; 17: 66.

[7] Chen W, Wang F, Yu X, Qi J, Dong H, Cui B, Zhang Q, Wu Y, An J, Ni N, Liu C, Han Y, Zhang S, Schmitt CA, Deng J, Yu Y and Du J. LncRNA MIR31HG fosters stemness malignant features of non-small cell lung cancer via H3K4me1- and H3K27Ace-mediated GLI2 expression. Oncogene 2024; 43: 1328-1340.

[8] Zhou Y, Fan Y, Zhou X, Mou A, He Y, Wang F and Liu Y. Significance of lncRNA MIR31HG in predicting the prognosis for Chinese patients with cancer: a meta-analysis. Biomark Med 2020; 14: 303-316.

[9] Huang HH, You GR, Tang SJ, Chang JT and Cheng AJ. Molecular signature of long noncoding RNA associated with areca nut-induced head and neck cancer. Cells 2023; 12: 873.

[10] Feng B, Chen K, Zhang W, Zheng Q and He Y. Silencing of lncRNA MIR31HG promotes nasopharyngeal carcinoma cell proliferation and inhibits apoptosis through suppressing the PI3K/AKT signaling pathway. J Clin Lab Anal 2022; 36: e24720.

[11] Gutwillig A, Santana-Magal N, Farhat-Younis L, Rasoulouniriana D, Madi A, Luxenburg C, Cohen J, Padmanabhan K, Shomron N, Shapira G, Gleiberman A, Parikh R, Levy C, Feinmesser M, Hershkovitz D, Zemser-Werner V, Zlotnik O, Kroon S, Hardt WD, Debets R, Reticker-Flynn NE, Rider P and Carmi Y. Transient cell-in-cell formation underlies tumor relapse and resistance to immunotherapy. Elife 2022; 11: e80315.

[12] Wang X, Li Y, Li J, Li L, Zhu H, Chen H, Kong R, Wang G, Wang Y, Hu J and Sun B. Cell-in-cell phenomenon and its relationship with tumor microenvironment and tumor progression: a review. Front Cell Dev Biol 2019; 7: 311.

[13] Almangush A, Mäkitie AA, Hagström J, Haglund C, Kowalski LP, Nieminen P, Coletta RD, Salo T and Leivo I. Cell-in-cell phenomenon associates with aggressive characteristics and cancer-related mortality in early oral tongue cancer. BMC Cancer 2020; 20: 843.

[14] Wang R, Zhu Y, Zhong H, Gao X, Sun Q and He M. Homotypic cell-in-cell structures as an adverse prognostic predictor of hepatocellular carcinoma. Front Oncol 2022; 12: 1007305.

[15] Borensztejn K, Tyrna P, Gaweł AM, Dziuba I, Wojcik C, Bialy LP and Mlynarczuk-Bialy I. Classification of cell-in-cell structures: different phenomena with similar appearance. Cells 2021; 10: 2569.

[16] Choe YJ, Min JY, Lee H, Lee SY, Kwon J, Kim HJ, Lee J, Kim HM, Park HS, Cho MY, Hyun JY, Kim HM, Chung YH, Ha SK, Jeong HG, Choi I, Kim TD, Hong KS and Han EH. Heterotypic cell-in-cell structures between cancer and NK cells are associated with enhanced anticancer drug resistance. iScience 2022; 25: 105017.

[17] Schenker H, Büttner-Herold M, Fietkau R and Distel LV. Cell-in-cell structures are more potent predictors of outcome than senescence or apoptosis in head and neck squamous cell carcinomas. Radiat Oncol 2017; 12: 21.

[18] Siquara da Rocha LO, Souza BSF, Coletta RD, Lambert DW and Gurgel Rocha CA. Mapping cell-in-cell structures in oral squamous cell carcinoma. Cells 2023; 12: 2418.

[19] Davies SP, Reynolds GM, Wilkinson AL, Li X, Rose R, Leekha M, Liu YS, Gandhi R, Buckroyd E, Grove J, Barnes NM, May RC, Hubscher SG, Adams DH, Huang Y, Qureshi O and Stamataki Z. Hepatocytes delete regulatory T cells by enclysis, a CD4(+) T cell engulfment process. Cell Rep 2019; 29: 1610-1620, e4.
[20] Fan J, Fang Q, Yang Y, Cui M, Zhao M, Qi J, Luo R, Du W, Liu S and Sun Q. Role of heterotypic neutrophil-in-tumor structure in the prognosis of patients with buccal mucosa squamous cell carcinoma. Front Oncol 2020; 10: 541878.
[21] Okuyama K, Fukushima H, Naruse T and Yanamoto S. Cell-in-cell structure in cancer: evading strategies from anti-cancer therapies. Front Oncol 2023; 13: 1248097.
[22] Davies SP, Terry LV, Wilkinson AL and Stamataki Z. Cell-in-cell structures in the liver: a tale of four E's. Front Immunol 2020; 11: 650.
[23] Demin S, Berdieva M and Goodkov A. Cell-cell fusions and cell-in-cell phenomena in healthy cells and cancer: lessons from protists and invertebrates. Semin Cancer Biol 2022; 81: 96-105.
[24] Johnson DE, Burtness B, Leemans CR, Lui VWY, Bauman JE and Grandis JR. Head and neck squamous cell carcinoma. Nat Rev Dis Primers 2020; 6: 92.
[25] Cai Y, Sheng Z, Dong Z and Wang J. EGFR inhibitor CL-387785 suppresses the progression of lung adenocarcinoma. Curr Mol Pharmacol 2023; 16: 211-216.
[26] Chakraborty R, Khodlan P, Tay A and Liu F. STAT3 interactome predicts presence of proteins that regulate immune system in oral squamous cell carcinoma. J Oral Biosci 2024; 66: 67-73.
[27] Tang YC, Hsiao JR, Jiang SS, Chang JY, Chu PY, Liu KJ, Fang HL, Lin LM, Chen HH, Huang YW, Chen YT, Tsai FY, Lin SF, Chuang YJ and Kuo CC. c-MYC-directed NRF2 drives malignant progression of head and neck cancer via glucose-6-phosphate dehydrogenase and transketolase activation. Theranostics 2021; 11: 5232-5247.
[28] Siquara da Rocha LO, Souza BSF, Lambert DW and Gurgel Rocha CA. Cell-in-cell events in oral squamous cell carcinoma. Front Oncol 2022; 12: 931092.
[29] Fais S and Overholtzer M. Cell-in-cell phenomena in cancer. Nat Rev Cancer 2018; 18: 758-766.
[30] Bauer MF, Hader M, Hecht M, Büttner-Herold M, Fietkau R and Distel LVR. Cell-in-cell phenomenon: leukocyte engulfment by non-tumorigenic cells and cancer cell lines. BMC Mol Cell Biol 2021; 22: 39.
[31] Mackay HL and Muller PAJ. Biological relevance of cell-in-cell in cancers. Biochem Soc Trans 2019; 47: 725-732.
[32] Hamann JC, Surcel A, Chen R, Teragawa C, Albeck JG, Robinson DN and Overholtzer M. Entosis is induced by glucose starvation. Cell Rep 2017; 20: 201-210.
[33] Ruan B, Zhang B, Chen A, Yuan L, Liang J, Wang M, Zhang Z, Fan J, Yu X, Zhang X, Niu Z, Zheng Y, Gu S, Liu X, Du H, Wang J, Hu X, Gao L, Chen Z, Huang H, Wang X and Sun Q. Cholesterol inhibits entotic cell-in-cell formation and actomyosin contraction. Biochem Biophys Res Commun 2018; 495: 1440-1446.
[34] Unseld LH, Hildebrand LS, Putz F, Büttner-Herold M, Daniel C, Fietkau R and Distel LV. Non-professional phagocytosis increases in melanoma cells and tissues with increasing e-cadherin expression. Curr Oncol 2023; 30: 7542-7552.
[35] Kyrysyuk O and Wucherpfennig KW. Designing cancer immunotherapies that engage T cells and NK cells. Annu Rev Immunol 2023; 41: 17-38.
[36] Huntington ND, Cursons J and Rautela J. The cancer-natural killer cell immunity cycle. Nat Rev Cancer 2020; 20: 437-454.
[37] Huang H, He M, Zhang Y, Zhang B, Niu Z, Zheng Y, Li W, Cui P, Wang X and Sun Q. Identification and validation of heterotypic cell-in-cell structure as an adverse prognostic predictor for young patients of resectable pancreatic ductal adenocarcinoma. Signal Transduct Target Ther 2020; 5: 246.
[38] Kapsetaki SE, Cisneros LH and Maley CC. Cell-in-cell phenomena across the tree of life. Sci Rep 2024; 14: 7535.
[39] Buenaventura RGM, Merlino G and Yu Y. Ez-metastasizing: the crucial roles of ezrin in metastasis. Cells 2023; 12.
[40] Barik GK, Sahay O, Paul D and Santra MK. Ezrin gone rogue in cancer progression and metastasis: an enticing therapeutic target. Biochim Biophys Acta Rev Cancer 2022; 1877: 188753.
[41] Fais S. Cannibalism: a way to feed on metastatic tumors. Cancer Lett 2007; 258: 155-164.
[42] Myers JA and Miller JS. Exploring the NK cell platform for cancer immunotherapy. Nat Rev Clin Oncol 2021; 18: 85-100.